SUPPORTING INFORMATION

Multi-emissive lanthanide-based coordination polymers for potential application as luminescent bar-codes.

Jinzeng Wang, Yan Suffren*, Carole Daiguebonne, Stéphane Freslon, Kevin Bernot, Guillaume Calvez, Laurent Le Pollès, Claire Roiland and Olivier Guillou*.

[a] Univ Rennes, INSA Rennes, ENSCR, CNRS UMR 6226 "Institut des Sciences Chimiques de Rennes", F-35000 Rennes, France.

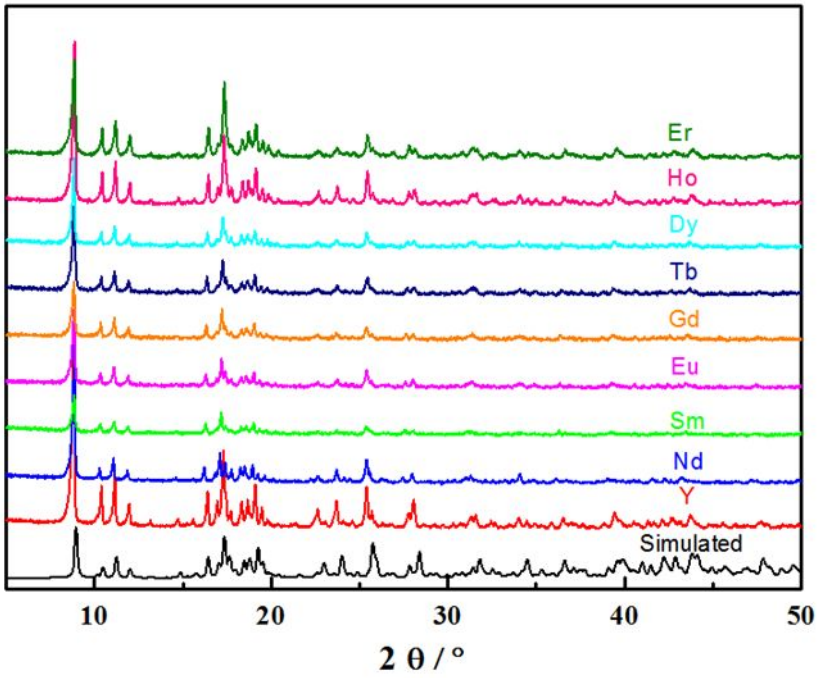

Figure S1. Experimental powder X-ray diffraction diagrams of $[Ln_2(mip)_3]_\infty$ with Ln = Nd - Er except Pm plus Y and simulated powder X-ray diffraction diagram of $[Y_2(mip)_3]_\infty$ on the basis of its crystal structure.

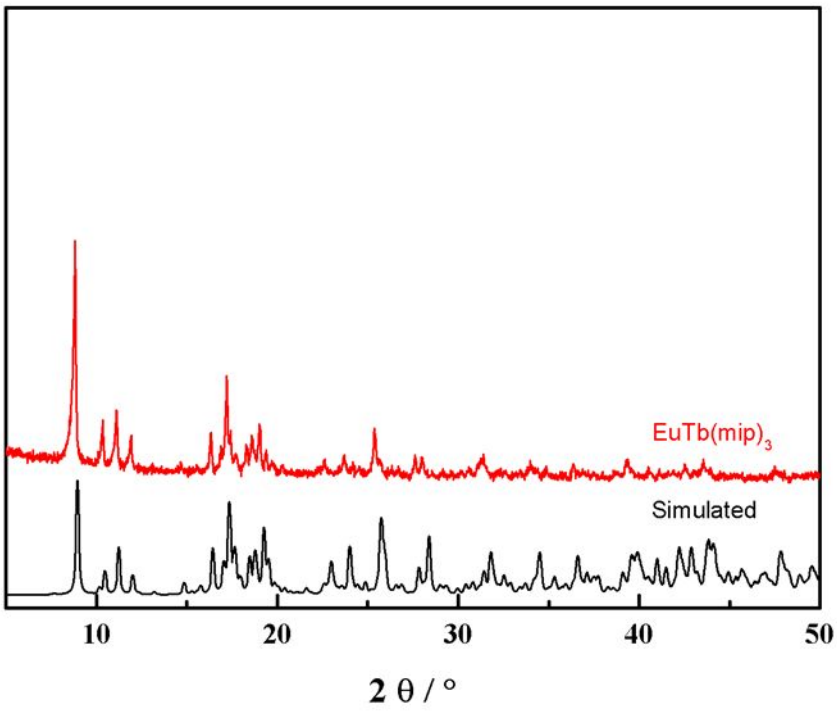

Figure S2. Experimental powder X-ray diffraction diagrams of $[EuTb(mip)_3]_\infty$ and simulated powder X-ray diffraction diagram of $[Y_2(mip)_3]_\infty$ on the basis of its crystal structure.

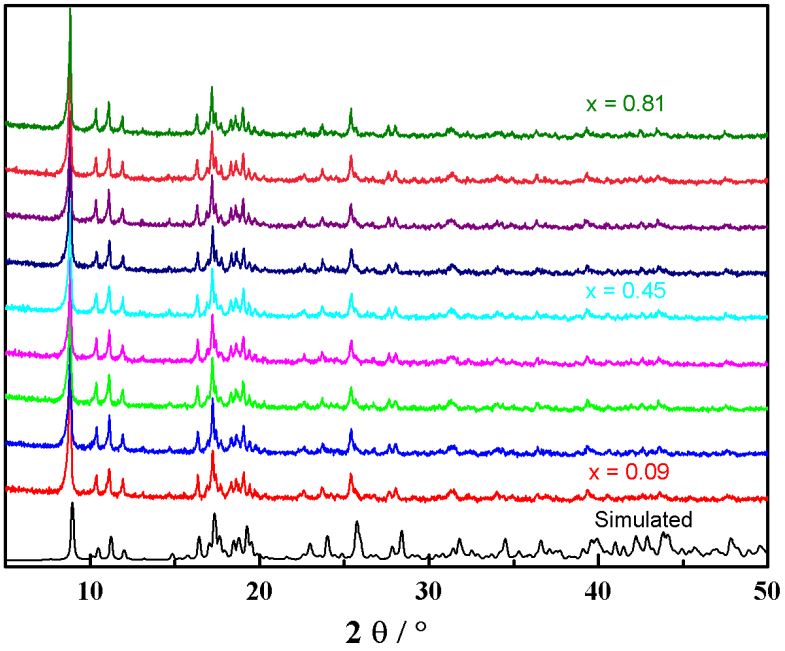

Figure S3. Experimental powder X-ray diffraction diagrams of $[Gd_{0.2}Eu_{2x}Tb_{1.8-2x}(mip)_3]_\infty$ with $0 \leq x \leq 0.9$ (stepwise 0.09) and simulated powder X-ray diffraction diagram of $[Y_2(mip)_3]_\infty$ on the basis of its crystal structure.

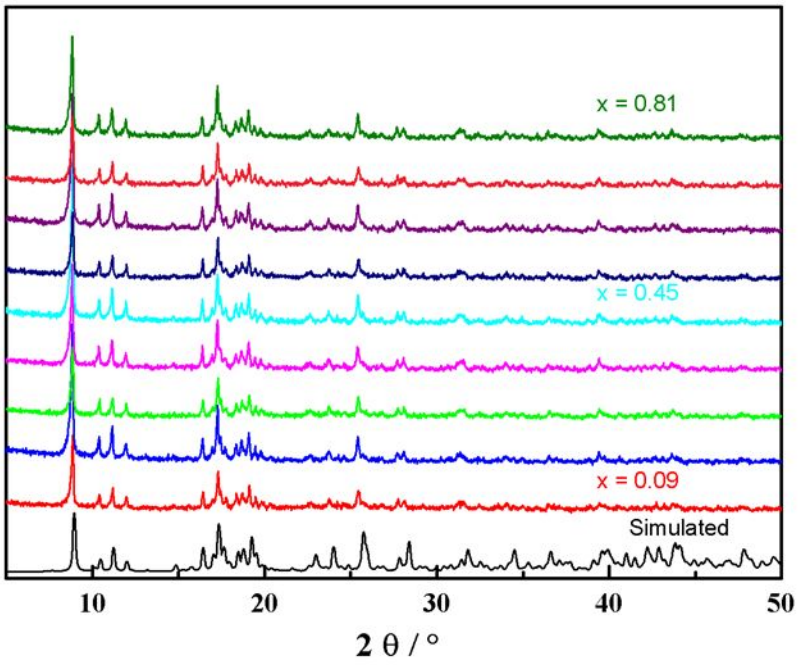

Figure S4. Experimental powder X-ray diffraction diagrams of $[Gd_{0.2}Dy_{2x}Tb_{1.8-2x}(mip)_3]_\infty$ with $0 \leq x \leq 0.9$ (stepwise 0.09) and simulated powder X-ray diffraction diagram of $[Y_2(mip)_3]_\infty$ on the basis of its crystal structure.

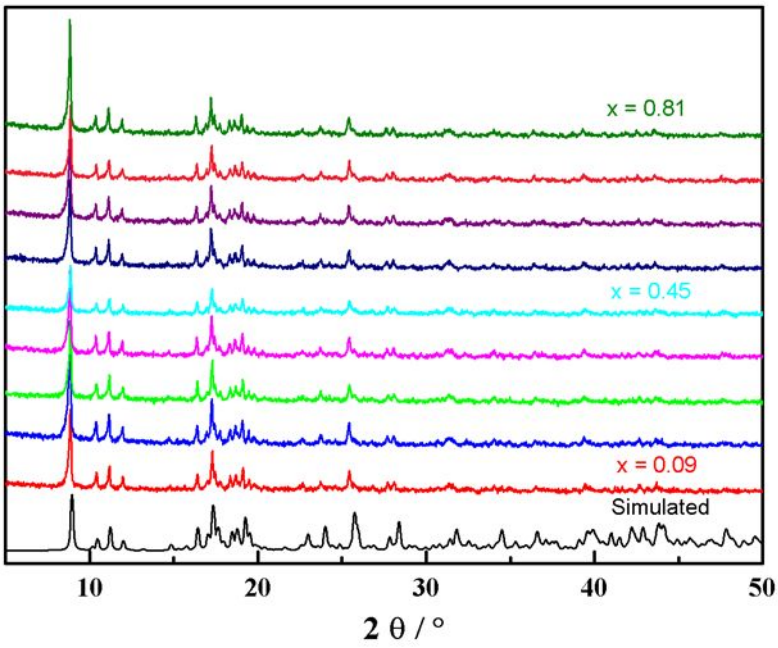

Figure S5. Experimental powder X-ray diffraction diagrams of $[Gd_{0.2}Dy_{2x}Eu_{1.8-2x}(mip)_3]_\infty$ with $0 \leq x \leq 0.9$ (stepwise 0.09) and simulated powder X-ray diffraction diagram of $[Y_2(mip)_3]_\infty$ on the basis of its crystal structure.

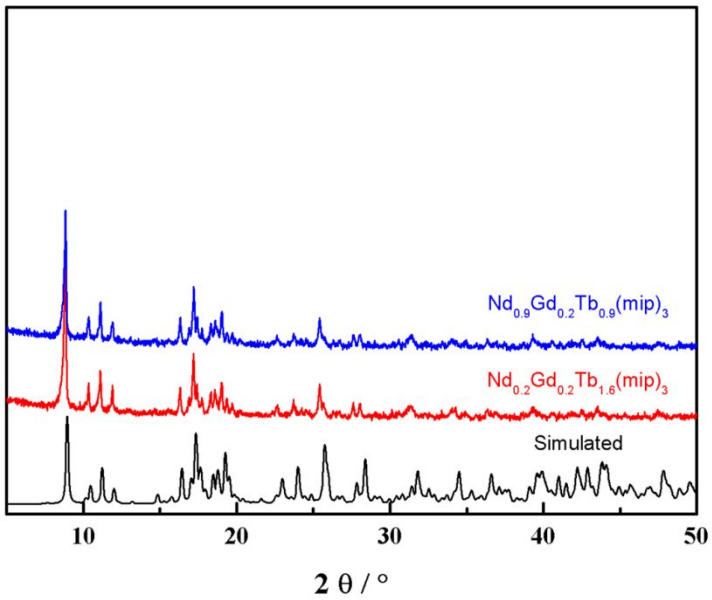

Figure S6. Experimental powder X-ray diffraction diagrams of $[Nd_{0.9}Gd_{0.2}Tb_{0.9}(mip)_3]_\infty$, $[Nd_{0.2}Gd_{0.2}Tb_{1.6}(mip)_3]_\infty$ and simulated powder X-ray diffraction diagram of $[Y_2(mip)_3]_\infty$ on the basis of its crystal structure.

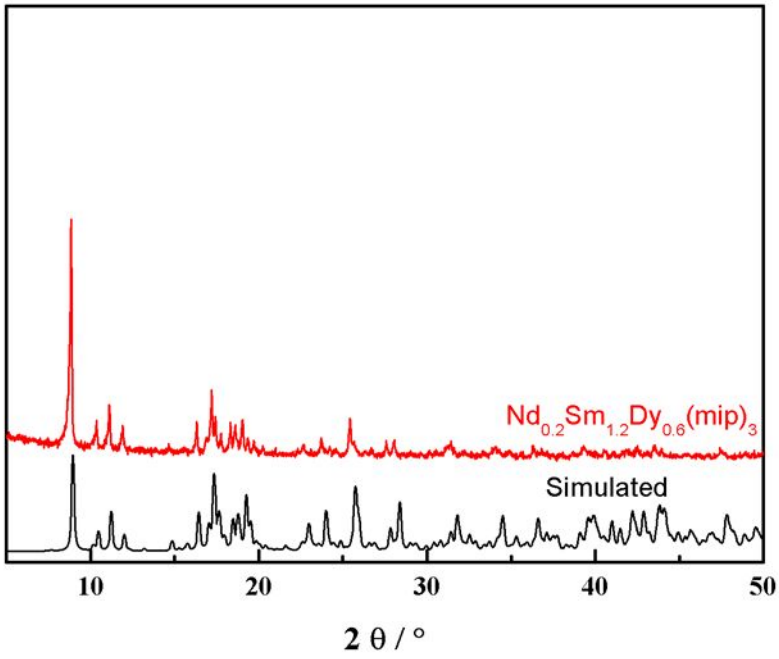

Figure S7. Experimental powder X-ray diffraction diagrams of $[Nd_{0.2}Sm_{1.2}Dy_{0.6}(mip)_3]_\infty$ and simulated powder X-ray diffraction diagram of $[Y_2(mip)_3]_\infty$ on the basis of its crystal structure.

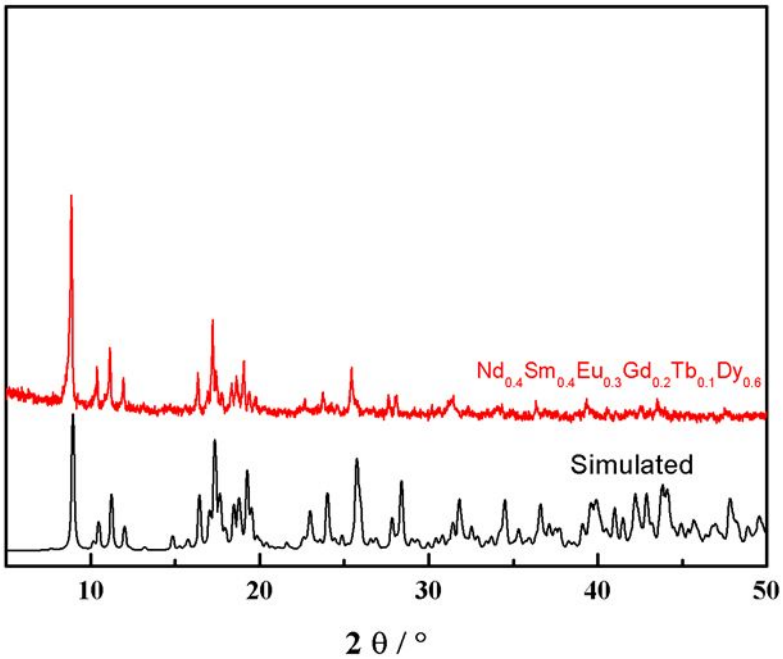

Figure S8. Experimental powder X-ray diffraction diagrams of $[Nd_{0.4}Sm_{0.4}Eu_{0.3}Gd_{0.2}Tb_{0.1}Dy_{0.6}(mip)_3]_\infty$ and simulated powder X-ray diffraction diagram of $[Y_2(mip)_3]_\infty$ on the basis of its crystal structure.

Table S1. Relative metallic contents measured by EDS.						
	% Gd	%Eu	%Tb			
$[EuTb(mip)_3]_\infty$	n/a	49(2)	51(2)			
$[Gd_{0.2}Eu_{2x}Tb_{1.8-2x}(mip)_3]_\infty$						
x = 0.09	9(2)	8(2)	83(2)			
x = 0.18	9(2)	19(2)	73(2)			
x = 0.27	10(2)	27(2)	63(2)			
x = 0.36	11(2)	35(2)	54(2)			
x = 0.45	11(2)	45(2)	44(2)			
x= 0.54	10(2)	53(2)	37(2)			
x= 0.64	10(2)	62(2)	28(2)			
x = 0.72	10(2)	71(2)	20(2)			
x= 0.81	11(2)	77(2)	12(2)			
$[Gd_{0.2}Dy_{2x}Tb_{1.8-2x}(mip)_3]_\infty$	%Gd	%Tb	%Dy			
x = 0.09	11(2)	79(2)	9(2)			
x = 0.18	9(2)	71(2)	20(2)			
x = 0.27	10(2)	62(2)	28(2)			
x = 0.36	10(2)	53(2)	37(2)			
x = 0.45	10(2)	45(2)	45(2)			
x= 0.54	9(2)	36(2)	55(2)			
x= 0.64	11(2)	27(2)	62(2)			
x = 0.72	10(2)	19(2)	72(2)			
x= 0.81	9(2)	11(2)	81(2)			
$[Gd_{0.2}Dy_{2x}Eu_{1.8-2x}(mip)_3]_\infty$	%Gd	%Eu	%Dy			
x = 0.09	13(2)	75(2)	12(2)			
x = 0.18	11(2)	66(2)	23(2)			
x = 0.27	11(2)	56(2)	33(2)			
x = 0.36	11(2)	47(2)	41(2)			
x = 0.45	12(2)	38(2)	50(2)			
x= 0.54	12(2)	31(2)	57(2)			
x= 0.64	11(2)	23(2)	66(2)			
x = 0.72	10(2)	13(2)	77(2)			
x= 0.81	9(2)	7(2)	84(2)			
	%Nd	%Gd	%Tb			
$[Nd_{0.9}Gd_{0.2}Tb_{0.9}(mip)_3]_\infty$	45(2)	10(2)	45(2)			
$[Nd_{0.2}Gd_{0.2}Tb_{1.6}(mip)_3]_\infty$	10(2)	11(2)	79(2)			
	%Nd	%Sm	%Dy			
$[Nd_{0.2}\ Sm_{1.2}Dy_{0.6}(mip)_3]_\infty$	10(2)	60(2)	30(2)			
	%Nd	%Sm	%Eu	%Gd	%Tb	%Dy
$[Nd_{0.4}Sm_{0.4}Eu_{0.3}Gd_{0.2}Tb_{0.1}Dy_{0.6}(mip)_3]_\infty$	20(2)	20(2)	13(2)	12(2)	5(2)	30(2)

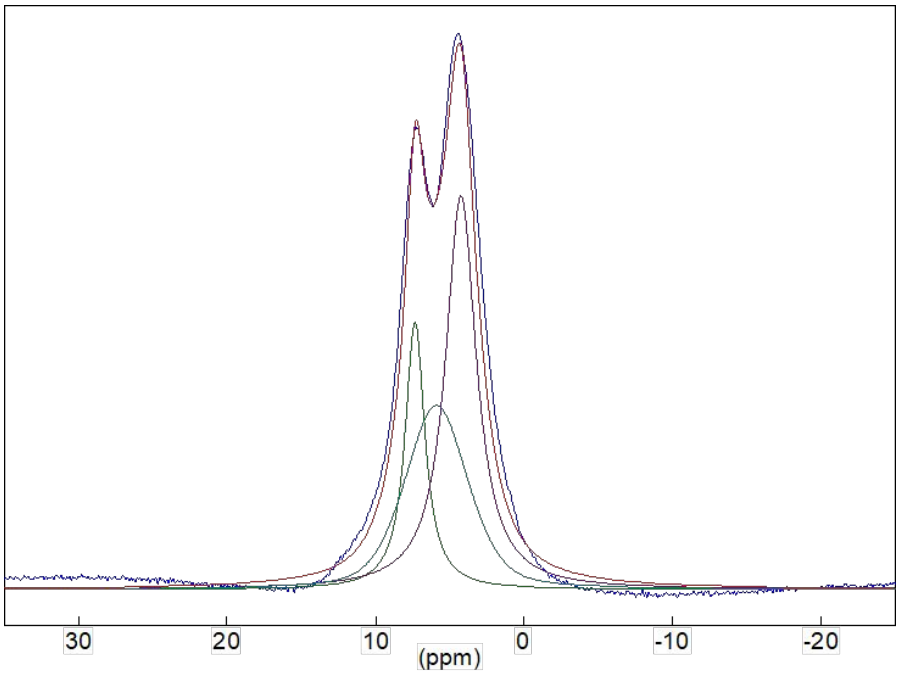

Figure S9. ^{1}H MAS NMR of $[Y_2(mip)_3]_\infty$ recorded at 14 T, using a 2.5 mm probe-head, spinning rate 30 kHz (blue). The spectrum was fitted (in red) with three components with relative intensities reflecting the contributions of three proton types (methyl, aromatic and water molecule protons, integrated intensities 9, 9, 24). (Dmfit software, D.Massiot, F.Fayon, M.Capron, I.King, S.Le Calvé, B.Alonso, J.O.Durand, B.Bujoli, Z.Gan, G.Hoatson, 'Modelling one and two-dimensional solid-state NMR spectra.', Magn. Reson. Chem. 40 70-76 (2002) doi:10.1002/mrc.984)

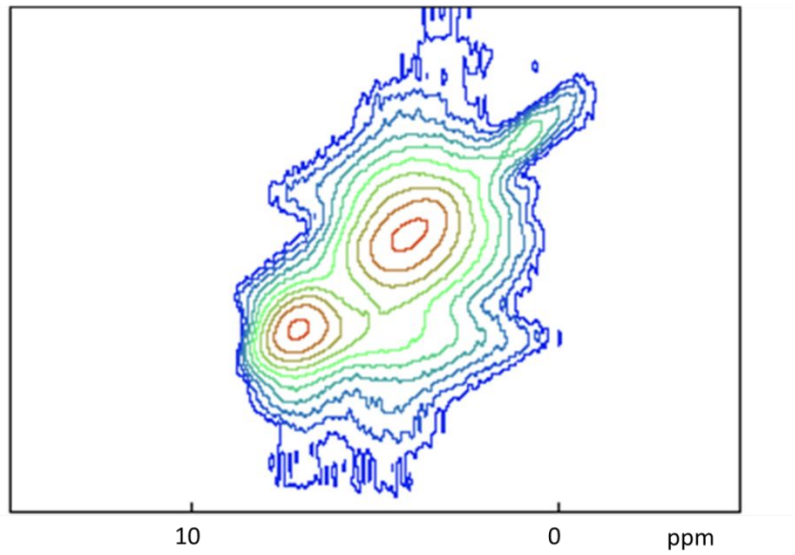

Figure S10. ^{1}H MAS NMR RFDR of $[Y_2(mip)_3]_\infty$. ^{1}H MAS NMR spectra were acquired at 14 T, using a 2.5 mm probe-head with a spinning rate of 30 kHz. RFDR experiments were carried out as described by Bennet, O. and Griffin, Vega J. (Chem. Phys. 98, 8624 (1992)) using a 5 rotor periods mixing time.

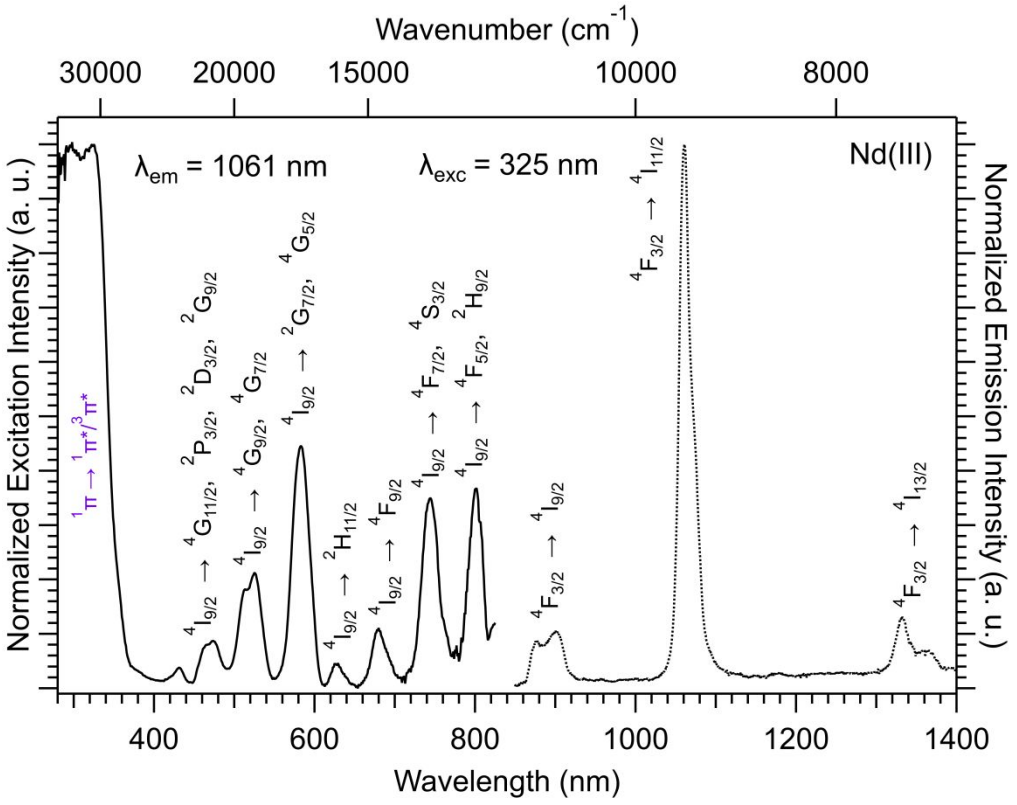

Figure S11. Excitation and emission spectra at room temperature of $[Nd_2(mip)_3]_\infty$.

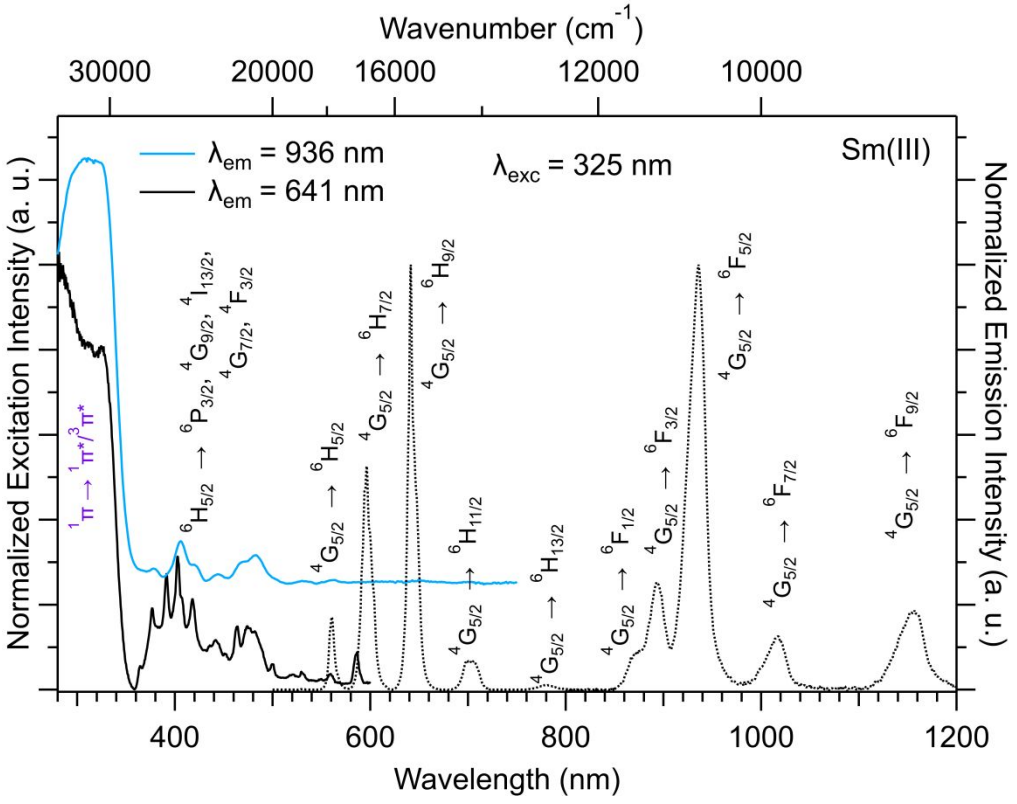

Figure S12. Excitation and emission spectra at room temperature of $[Sm_2(mip)_3]_\infty$.

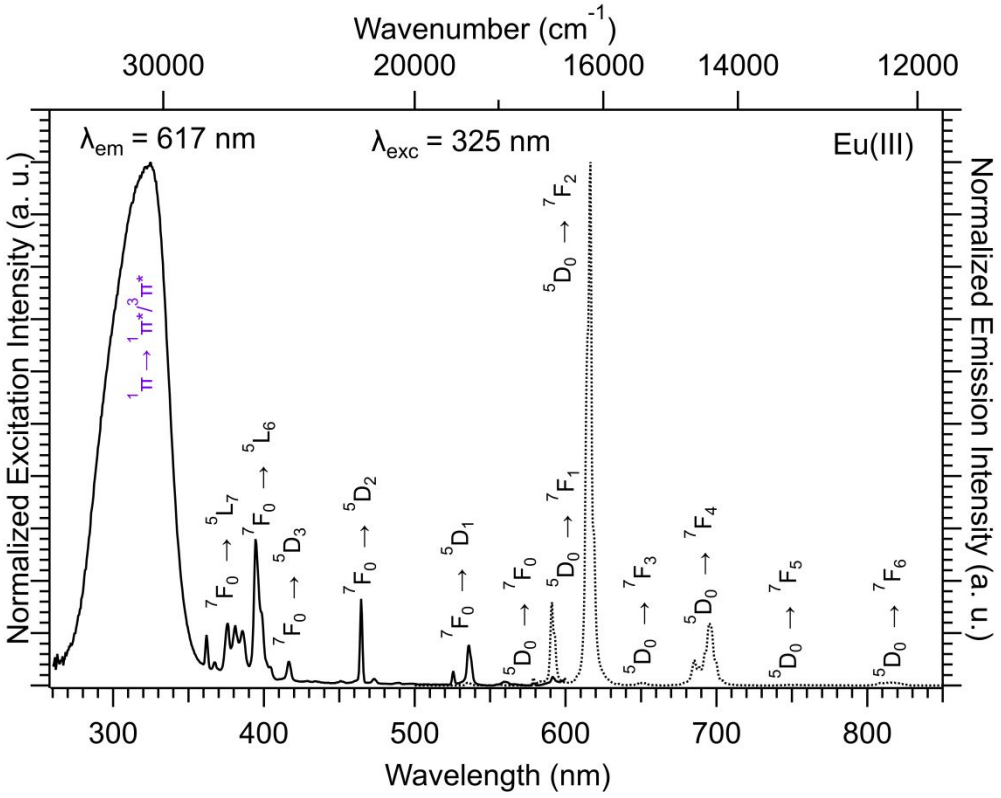

Figure S13. Excitation and emission spectra at room temperature of $[Eu_2(mip)_3]_\infty$.

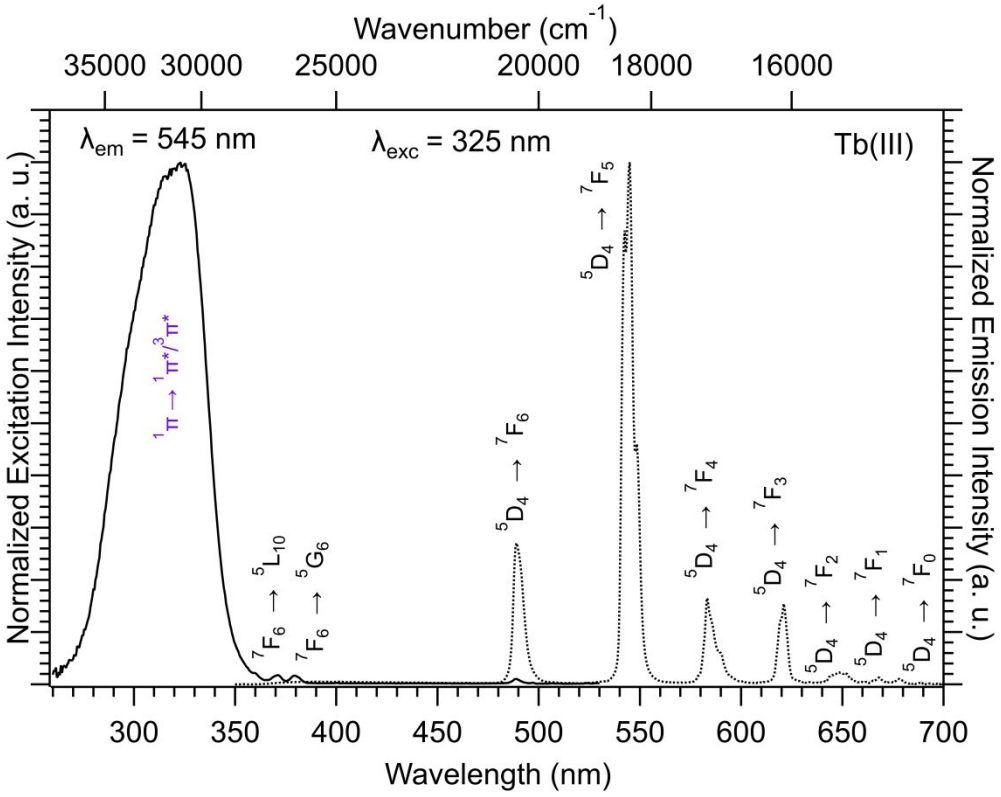

Figure S14. Excitation and emission spectra at room temperature of $[Tb_2(mip)_3]_\infty$.

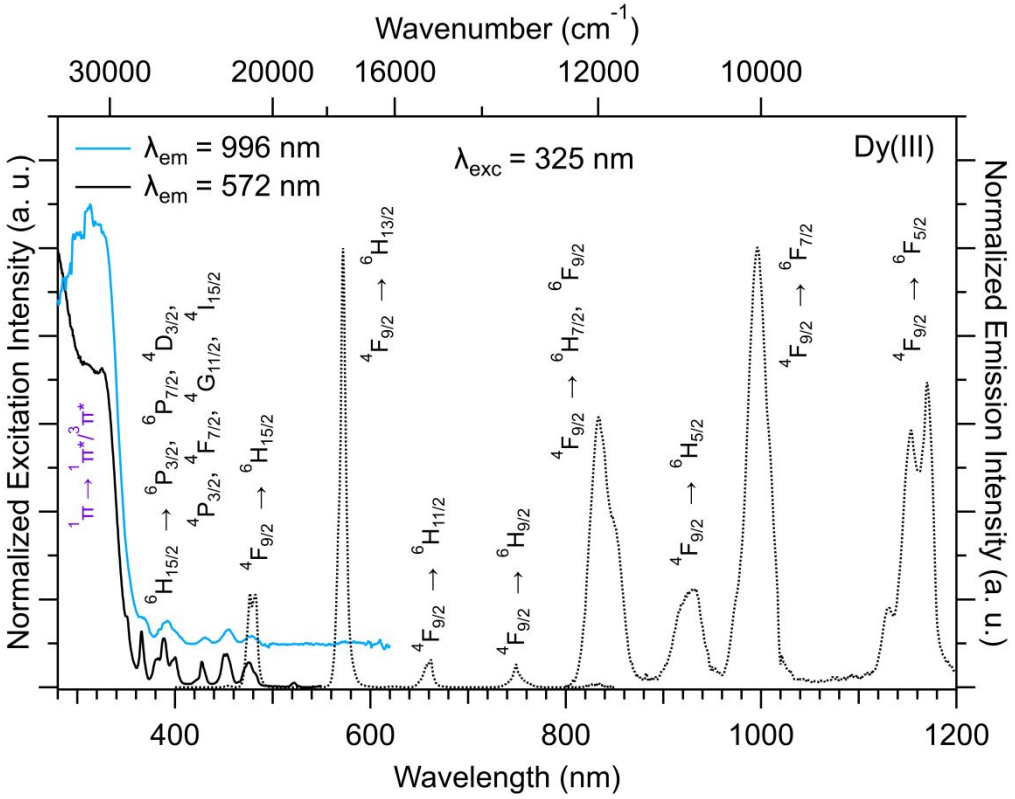

Figure S15. Excitation and emission spectra at room temperature of $[Dy_2(mip)_3]_\infty$.

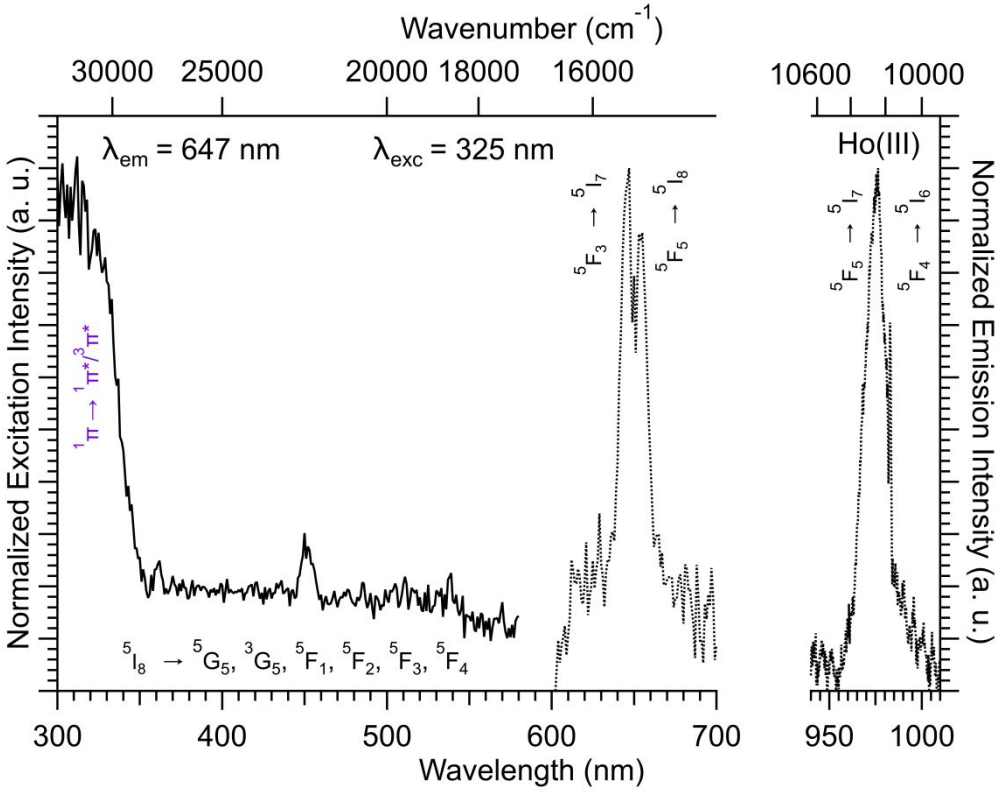

Figure S16. Excitation and emission spectra at room temperature of $[Ho_2(mip)_3]_\infty$.

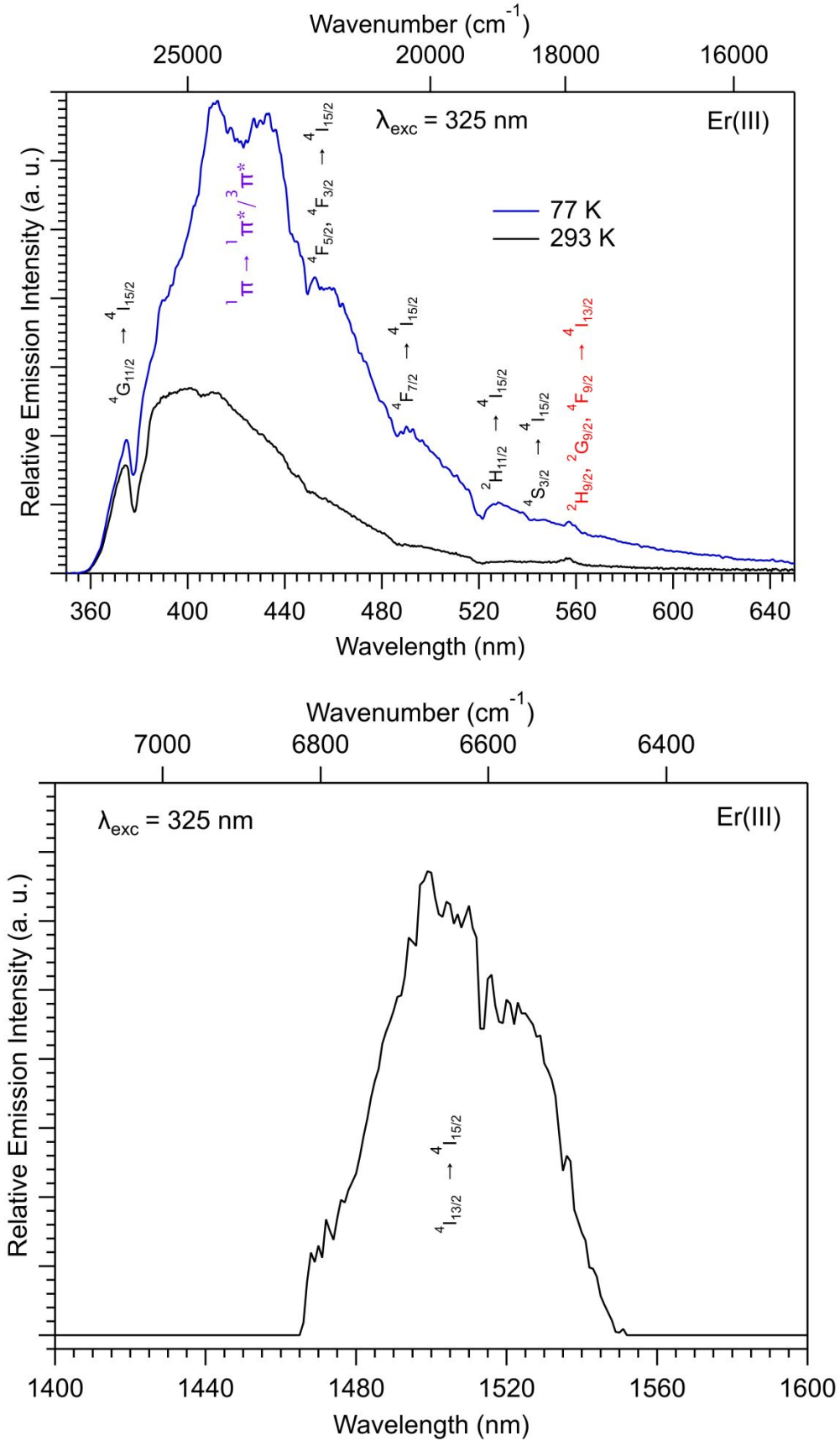

Figure S17. Visible emission spectra at 77 K (blue curve) and room temperature (black curve) of $[Er_2(mip)_3]_\infty$ (top). IR emission spectrum at 77 K of $[Er_2(mip)_3]_\infty$ (bottom).

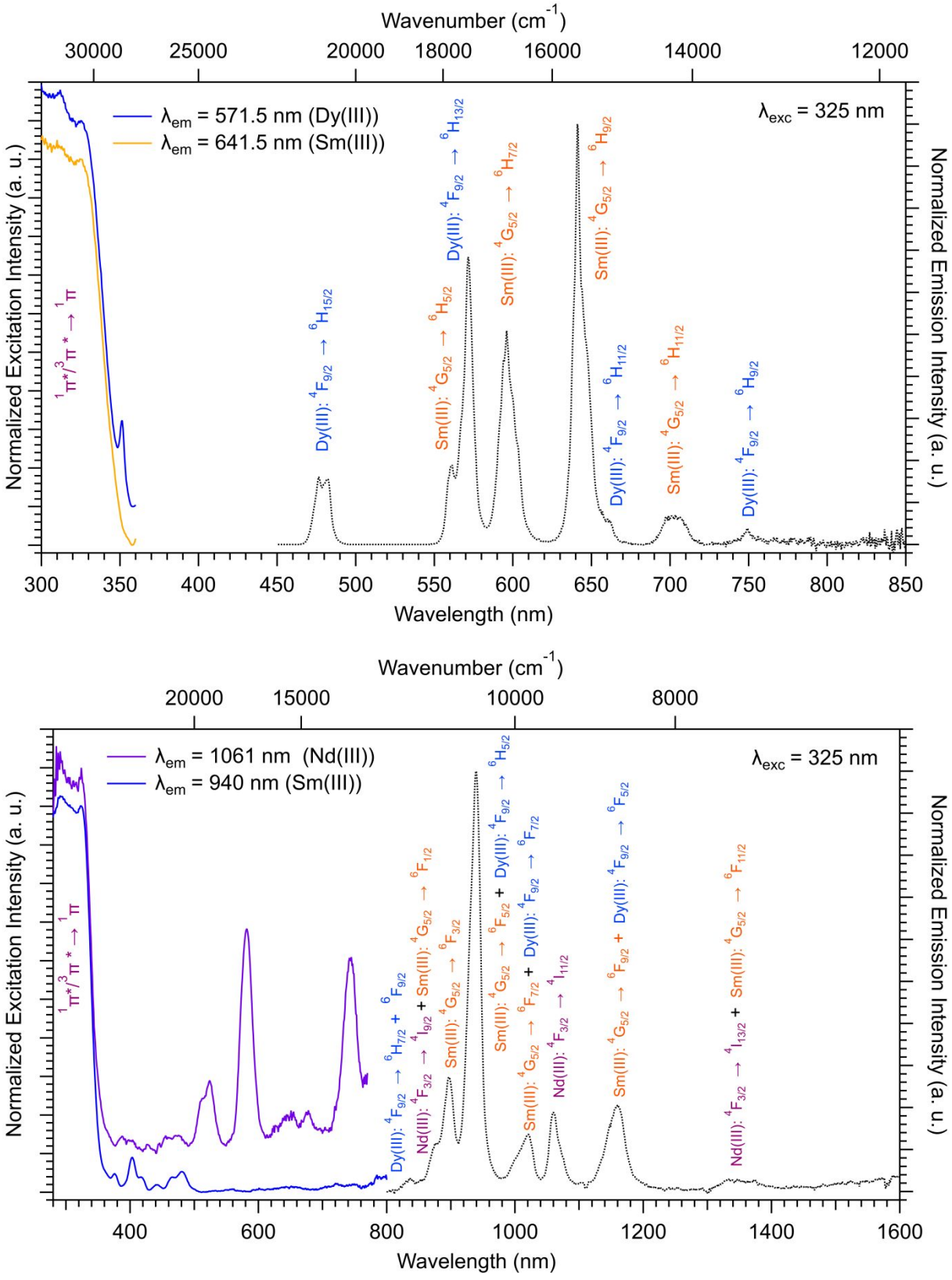

Figure S18. Room temperature solid state excitation and emission spectra of $[Nd_{0.2}Sm_{1.2}Dy_{0.6}(mip)_3]_\infty$ in the visible (top) and IR (bottom) regions.

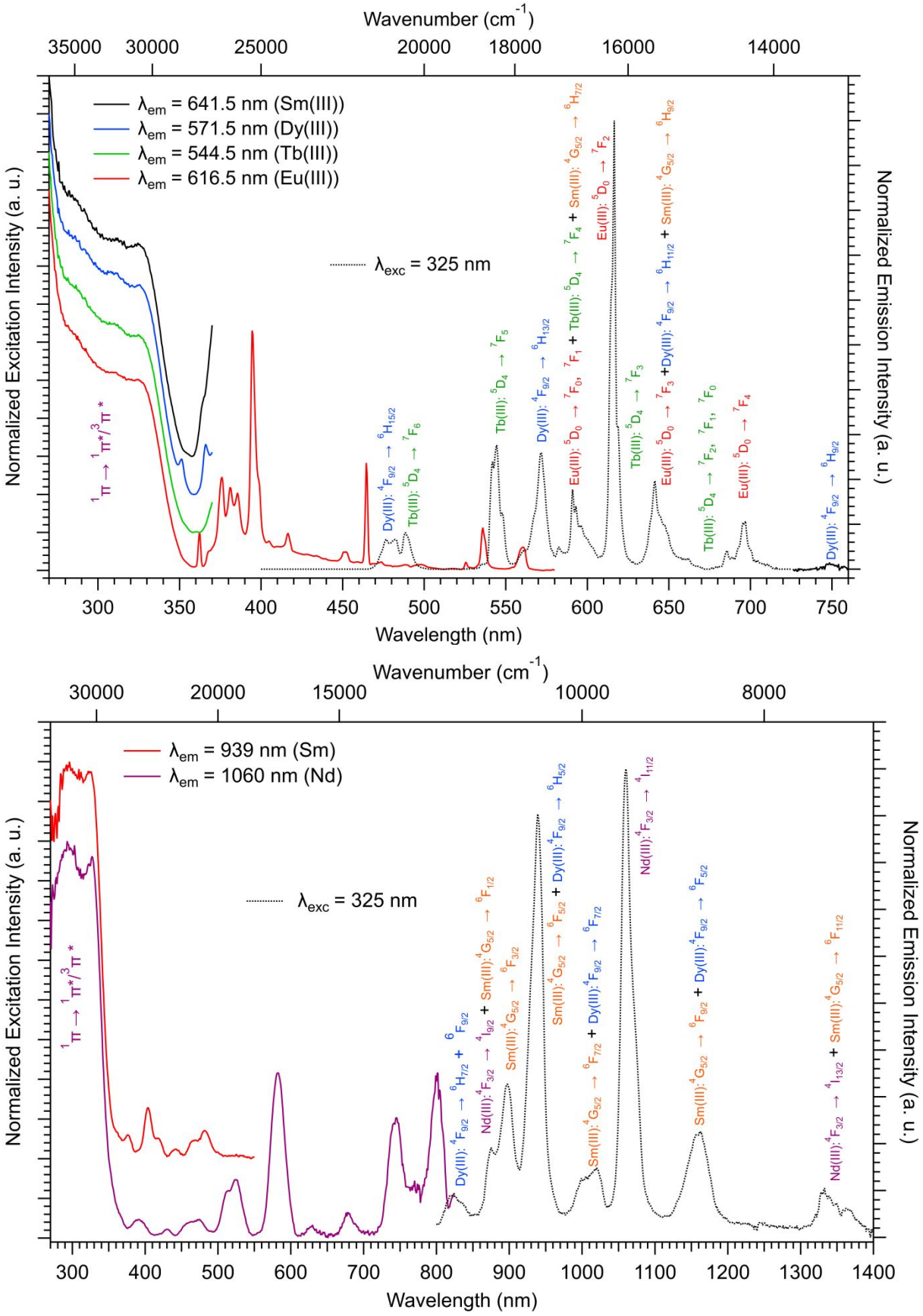

Figure S19. Room temperature solid state excitation and emission spectra of $[Nd_{0.4}Sm_{0.4}Eu_{0.3}Gd_{0.2}Tb_{0.1}Dy_{0.6}(mip)_3]_\infty$ in the visible (top) and Infra-Red (bottom) regions.

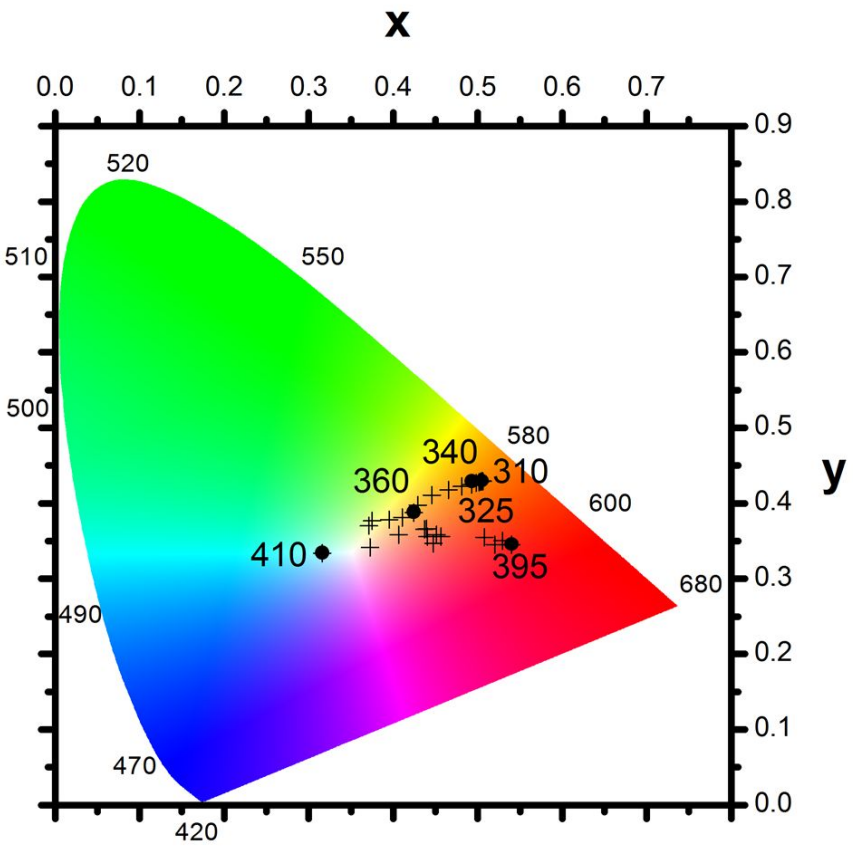

Figure S20. Calculated colorimetric coordinates of $[Nd_{0.4}Sm_{0.4}Eu_{0.3}Gd_{0.2}Tb_{0.1}Dy_{0.6}(mip)_3]_\infty$ *versus* excitation wavelength at room temperature. Referenced excitation wavelengths (λ_{exc} = 310 - 410 nm) correspond to excitation from ligand at 325 nm, and from direct f-f irradiation of Tb(III) at 340 nm, Dy(III) at 360 nm and Eu(III) at 395 nm.

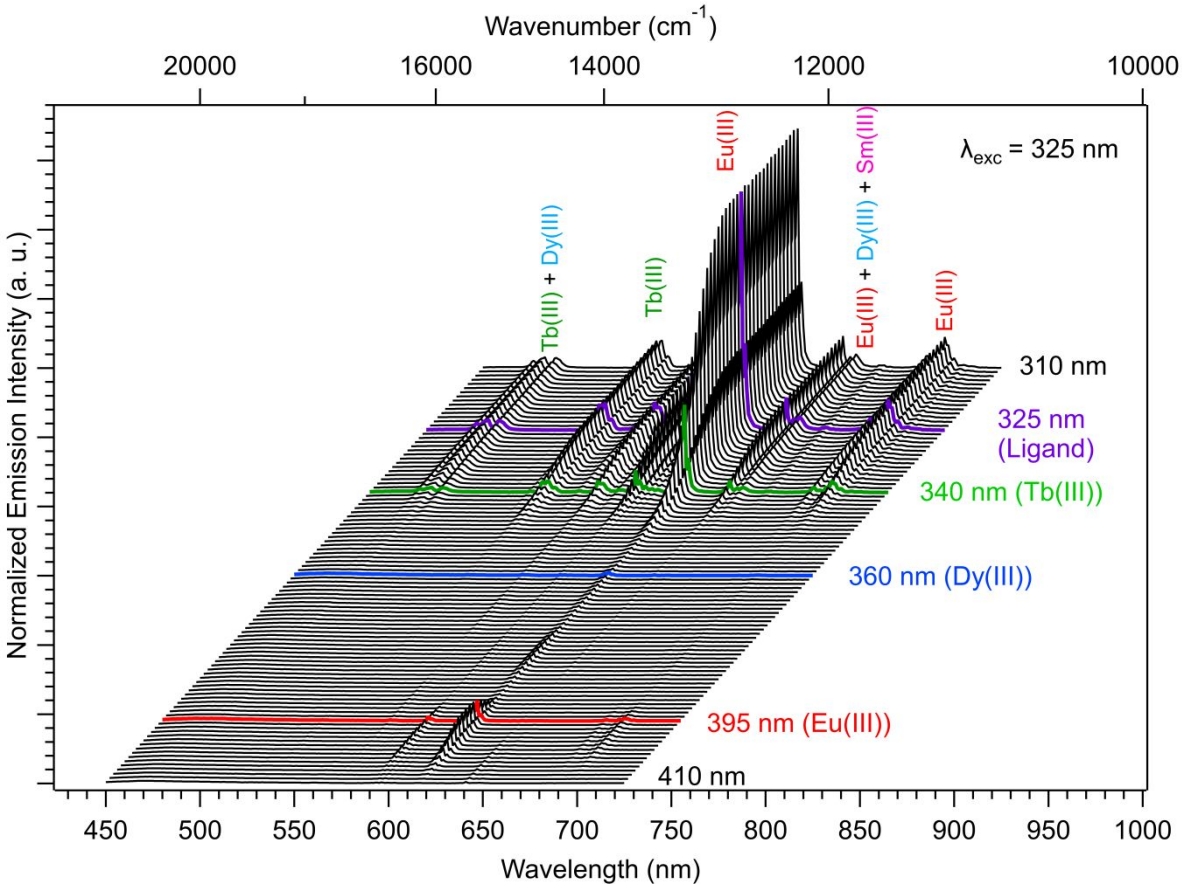

Figure S21. Emission spectra *vs* excitation wavelength of $[Nd_{0.4}Sm_{0.4}Eu_{0.3}Gd_{0.2}Tb_{0.1}Dy_{0.6}(mip)_3]_\infty$ at 77 K in the visible region. Referenced excitation wavelengths correspond to excitation from ligand at 325 nm, and from direct f-f irradiation of Tb(III) at 340 nm, Dy(III) at 360 nm and Eu(III) at 395 nm.

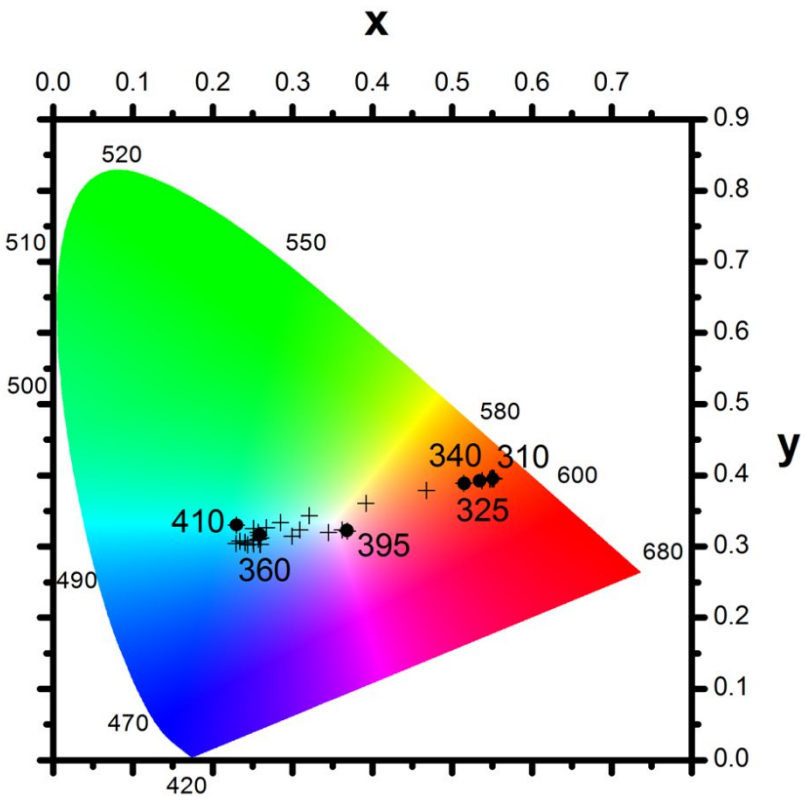

Figure S22. Calculated colorimetric coordinates of $[Nd_{0.4}Sm_{0.4}Eu_{0.3}Gd_{0.2}Tb_{0.1}Dy_{0.6}(mip)_3]_\infty$ *versus* excitation wavelength at 77 K. Referenced excitation wavelengths (λ_{exc} = 310 - 410 nm) correspond to excitation from ligand at 325 nm, and from direct f-f irradiation of Tb(III) at 340 nm, Dy(III) at 360 nm and Eu(III) at 395 nm.

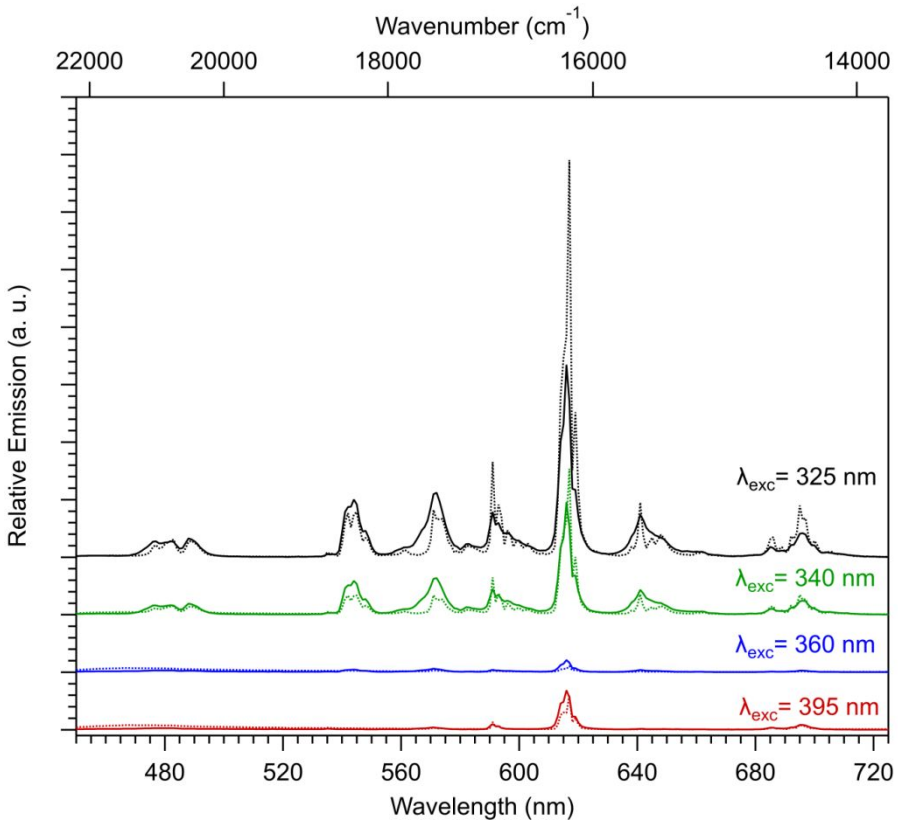

Figure S23. Solid state emission spectra of $[Nd_{0.4}Sm_{0.4}Eu_{0.3}Gd_{0.2}Tb_{0.1}Dy_{0.6}(mip)_3]_\infty$ in the visible under different excitation wavelength (from ligand at 325 nm, and from direct f-f irradiation of Tb(III) at 340 nm, Dy(III) at 360 nm and Eu(III) at 395 nm) at room-temperature (solid curves) and 77 K (dotted curves).